Real-time Sensorless Temperature Estimation of Lithium-ion Batteries Based on Online Operando Impedance Acquisition

Zheng, Yusheng; Che, Yunhong; Guo, Jia; Weinreich, Nicolai Andre; Kulkarni, Abhijit; Nadeem, Ahsan; Sui, Xin; Teodorescu, Remus

Published in:
IEEE Transactions on Power Electronics

DOI (link to publication from Publisher):
10.1109/TPEL.2024.3424267

Publication date:
2024

Document Version
Accepted author manuscript, peer reviewed version

Real-time Sensorless Temperature Estimation of Lithium-ion Batteries Based on Online Operando Impedance Acquisition

Yusheng Zheng, *Student Member, IEEE*, Yunhong Che, *Member, IEEE,* Jia Guo, Nicolai André Weinreich, *Student Member, IEEE*, Abhijit Kulkarni, *Member, IEEE*, Ahsan Nadeem, *Member, IEEE,* Xin Sui, *Member, IEEE*, Remus Teodorescu, *Fellow, IEEE*

***Abstract*—To guarantee safe, efficient, and reliable operations of lithium-ion battery (LIB) systems, it is indispensable to monitor their state of temperature (SOT). However, subject to limited onboard temperature sensors and the challenges in measuring battery internal temperature, the directly available temperature information in a battery system is extremely insufficient. To this end, developing sensorless temperature estimation techniques to obtain the temperature of each cell is important. This article proposes an operando impedance-based method to estimate the volume-averaged temperature of LIB in real time under dynamic operating conditions. A generalized rule for selecting optimal impedance parameters has been revealed for the first time through a comprehensive analysis of the electrochemical impedance spectroscopy (EIS) from different batteries. This rule can greatly reduce the time and effort to select optimal impedance parameters of the target cell for temperature estimations. The selected impedance parameters are then measured intermittently during battery operations via active pulse current injection, which allows the impedance acquisition under both loading and resting conditions. An estimation framework based on long short-term memory recurrent neural network (LSTM-RNN) has been proposed by taking advantage of the measured operando impedance, time-series current and voltage data to achieve real-time temperature estimation, which distinguishes this work from existing impedance-based methods. The proposed methodology has been experimentally validated against different batteries and operating conditions, with the root mean square error (RMSE) of the estimations within 0.46 ℃ for all cases.**

***Index Terms*—Lithium-ion batteries, temperature monitoring, operando impedance, optimal impedance parameters, pulse current**

This work was supported by the Villum Foundation for Smart Battery project (No. 222860), Independent Research Fund Denmark (No. 4263-00002B), and OPENSRUM grant from MSCA-IF European Commission (No. 223286) (Corresponding author: Yunhong Che).

Yusheng Zheng, Yunhong Che, Nicolai André Weinreich, Abhijit Kulkarni, Ahsan Nadeem, Xin Sui, Remus Teodorescu are with the Department of Energy, Aalborg University, Aalborg 9220, Denmark (e-mail: yzhe@energy.aau.dk, ych@energy.aau.dk, nawe@energy.aau.dk; eku@energy.aau.dk; ahna@energy.aau.dk; xin@energy.aau.dk; ret@energy.aau.dk)

Jia Guo is with the Department of Mechanical Engineering, Imperial College London, London SW7 2AZ, UK (e-mail: jia.guo1@imperial.ac.uk)

I. Introduction

As a key enabling technology to achieve net zero emissions, LIBs are now being widely applied in many large-scale applications including electric vehicles (EVs) [1], electric aircraft [2], and grid storage [3], thanks to their superiority in energy/power density, cycle life, charge/discharge efficiency. Nevertheless, the negative impacts of temperatures on the safety, performance, and lifetime of LIBs bring challenges to devising advanced battery management. Too high or too low temperatures negatively affect batteries' operations by triggering safety issues such as thermal runaway or performance degradation [4], [5]. Such thermal issues become even more complicated in large-scale battery applications, as thermal imbalance is exacerbated by inhomogeneous heating/cooling, particularly under aggressive usage scenarios. Therefore, how to manage a battery system to counteract such negative thermal effects is critical to unleashing its full potential, where monitoring the SOT of each cell is essential [6].

Traditionally, the cell temperature can be monitored via sensors such as thermistors or thermocouples attached to the cell surface [7]. Nevertheless, given the large number of battery cells in a system, allocating temperature sensors to each cell will substantially increase the cost and hardware complexity. As a result, only limited temperature sensors are installed at some key locations to monitor the cell temperature (e.g., 16 for 288 cells in Chevy Volt and 10 for 76 cells in Ford C-max Hybrid), and such sparse temperature sensing makes it difficult to achieve full observability of the temperature in each cell [8]. Furthermore, even with a surface temperature sensor, the fast-varying internal temperature of the cell cannot be tracked in time owing to the heat transfer delay from the core to the surface. For many battery systems, the amount of temperature information that can be obtained via direct sensor measurement is very limited, which leads to suboptimal management of the whole system [6]. To compensate for such deficiency in temperature information, it is of paramount importance to extract the temperature information of those cells without surface-mounted temperature sensors.

There are three typical methods in the existing literature to achieve sensorless temperature estimation, including thermal model-based estimation, data-driven estimation, and impedance-based estimation. In thermal model-based estimation, various control-oriented thermal models such as thermal equivalent circuit (TEC) models [9], [10], polynomial approximation (PA) models [11], and spectral-Galerkin models [12], have been developed to achieve efficient computations for onboard applications. Battery temperature is treated as one of the internal states and monitored by the observer developed based on these thermal models and filtering techniques (e.g., Kalman filter) [13], [14]. However, thermal model-based estimation often falls into the dilemma of model accuracy, computational complexity, and parameterization difficulty [6]. In addition, the observability of the cell temperature is another issue when designing the observer without temperature-related signals (e.g., surface temperature) as the feedback. Data-driven estimations, attempt to take advantage of the nonlinear mapping capabilities of machine learning algorithms to estimate the battery temperature through current, voltage, SOC, and ambient temperatures [15], [16]. Nevertheless, owing to the weak correlation between cell temperature and its voltage, the accuracy and generalization capability of the traditional data-driven estimation can hardly be guaranteed [16], [17], [18].

EIS has become an emerging non-invasive tool to achieve state estimation, charging control, and fault diagnosis as it provides abundant information regarding battery internal dynamics in the frequency domain [19], [20]. Particularly, in impedance-based temperature estimations, by calibrating the impedance-temperature relationship at certain frequencies where some impedance parameters (e.g., real part, imaginary part, magnitude, or phase) are sensitive to temperature but insensitive to state of charge (SOC) and state of health (SOH), the volume-average temperature of the cell can be estimated by measuring the impedance [21], [22], [23], [24], [25]. Srinivasan et al. found that the phase shift of the impedance between 40-100 Hz exhibits a monotonic trend with the cell temperature [26]. Richardson et al. applied the real part of the impedance at 215 Hz to estimate the volume-average temperature of the cell [22]. Other examples of impedance-based temperature estimation can be summarized in ref. [6], [18], [20].

Despite extensive studies on impedance-based temperature estimation using different impedance parameters and frequencies, the estimation under dynamic battery operations has seldom been investigated. Most works only use the impedance and battery temperature measured after long relaxation for model development and validation, which limits the model's applicability during dynamic power applications. The research gaps in the existing literature can be summarized as follows: (1) A generalized rule for selecting optimal impedance parameters is still lacking, which impedes quick parameter selection and fast model development. In existing studies, there is no underlying consensus on which is the optimal impedance parameter for temperature estimation. Each conclusion is made based on a large EIS dataset of the target cell, which is time-consuming to obtain via lab tests, while the conclusion is often difficult to generalize to other cells with different formats or chemistries. (2) Applying the impedance-temperature relationship parameterized at the close-to-equilibrium status to the temperature estimation during cell operations will lead to increased estimation errors [27]. The reason is that the impedance measured after sufficient relaxation (i.e., classical impedance) is different from that measured during cell operations (i.e., operando impedance) since in the latter case the linearity and stationarity can hardly be guaranteed [28], [29]. (3) How to measure the selected optimal impedance parameters timely and achieve real-time temperature estimation under highly dynamic cycles remains unexplored, particularly when batteries are under load conditions. In real-world applications, it is impractical to interrupt the battery operations and wait for a long period to perform impedance measurements. As such, developing an online impedance acquisition method under load conditions is critical to real-time SOT monitoring.

To bridge the aforementioned research gaps, this paper investigates the online implementation of impedance-based temperature estimation comprehensively, including the optimal impedance parameter selection, online impedance acquisition, and the real-time temperature estimation framework. The main contributions are summarized as follows: (1) A generalized rule for fast impedance parameter selection has been concluded, which uncovers the common characteristics of optimal impedance parameters of different battery chemistries and formats. This rule helps select optimal impedance parameters for temperature estimation more efficiently without the need to collect a large amount of EIS data from the target cell. (2) A methodology for measuring the selected impedance parameters under highly dynamic load conditions has been proposed based on active pulse current injection, which enables instantaneous impedance measurement at the desired frequency without interrupting battery operations. (3) Since it is not practical to measure the operando impedance every second during battery operations, a data-driven temperature estimation framework is proposed by leveraging the intermittently acquired operando impedance as well as the time-series current and voltage data to achieve accurate and real-time estimation of battery temperature, enabling continuous monitoring of battery SOT.

The remaining parts of this work are organized as follows. Section II introduces the proposed real-time impedance-based temperature estimation framework. Section III describes the experimental setups. Section IV elucidates the EIS analysis and the characteristics of optimal impedance parameters. Then, the operando impedance acquisition and the corresponding temperature estimation are presented in Section V, followed by the conclusion and future work in Section VI.

II. METHODOLOGY

The classical electrochemical impedance of a battery can be measured with a sufficiently small current or voltage disturbance at specific frequencies and the corresponding response, which is expressed as,

$$Z(j\omega)=\frac{V(j\omega)}{I(j\omega)}=|Z(\omega)|e^{j\angle Z(\omega)}=Z'(\omega)+jZ''(\omega) \quad (1)$$

with $j\omega=j2\pi f$, where f is the frequency of the disturbance, j is the imaginary number, $|Z|$ and $\angle Z$ are the magnitude and phase of the impedance, Z' and Z'' are the real and imaginary parts of the impedance. By sweeping the frequency

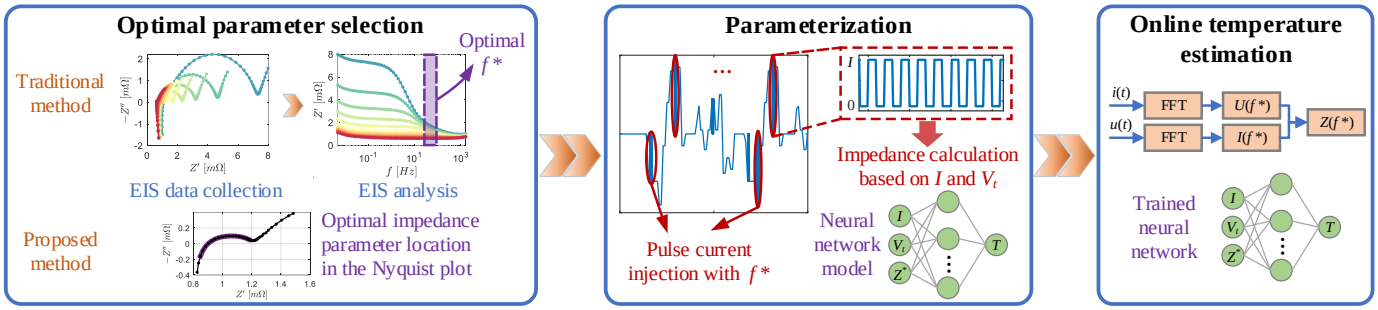

Fig. 1. Flowchart of impedance-based battery temperature estimation.

over a range, the whole impedance spectrum (i.e., EIS) can be obtained.

A typical framework for impedance-based temperature estimation with pulse current-enabled impedance acquisition can be illustrated in Fig. 1. Firstly, the optimal impedance parameters for temperature estimation should be carefully selected in order to achieve accurate and robust estimation. Traditionally, the classical EIS data of the battery under different temperatures and SOCs needs to be collected, where time-invariance and linearity should be guaranteed during the measurement. The EIS data will be analyzed in terms of its dependence on temperature and SOC, and then impedance parameters with optimal frequencies f^* will be selected under which they are sensitive to temperature but insensitive to SOC. Normally, a single-frequency impedance will be used for temperature estimation because it allows instantaneous acquisition for timely temperature estimation, without the need to know the whole spectrum [24], [25], [30], [31]. Nevertheless, the traditional impedance parameter selection method typically requires the EIS dataset of the target cell, which is time-consuming to collect. In addition, different battery types may have different impedance characteristics, making it difficult for the selected impedance parameters from one cell to be applied to other cells.

In this work, we aim to make the optimal impedance parameter selection process more efficient by finding a generalized impedance parameter selection rule that is effective for different batteries, which to the best of the authors' knowledge is lacking in the existing literature. In this way, instead of collecting a considerable EIS dataset, the optimal impedance parameters can be selected efficiently based on only one impedance spectrum of the target battery. It should be noted that only the short-term impedance characteristics of the battery are considered in this study. The effect of battery degradation on the impedance change is quite complicated and needs to be further investigated.

With the optimal impedance parameter selected, the temperature estimation model needs to be parameterized. The classical impedance of the cell can be modeled as a function of frequency, temperature, and SOC, as given by

$$Z = g\left(f, T_{avg}, SOC\right) \tag{2}$$

where T_{avg} is the volume-averaged temperature of the cell. Under f^*, the SOC dependence of the impedance can be neglected, and the impedance can be expressed as,

$$Z^* \approx g\left(T_{avg}\right)\Big|_{f=f^*} \tag{3}$$

In this way, the temperature estimation function can be obtained through the inverse function of Eq. (3) as,

$$\hat{T}_{avg} = g^{-1}\left(Z^*\right) \tag{4}$$

Nevertheless, such a relationship parameterized offline via classical impedance might fail under dynamic loading conditions since the operando impedance obtained online is different from the classical impedance even under the same SOC and temperature. As such, the temperature estimation function must be parameterized through the operando impedance at the frequency of f^*. In this article, in order to measure the operando impedance during dynamic battery operations, a new methodology is proposed by injecting a short-period pulse current at the frequency of f^* and recording the current and voltage responses. The operando impedance during this short excitation period can be calculated based on the fast Fourier transformation (FFT) of the measured current and voltage. Since stationarity and linearity are not guaranteed during this measurement, the measured impedance at f^* not only depends on the cell temperature but also on loading conditions (e.g., current amplitude and directions). Therefore, a neural network model is used to capture the mapping relationship between the input (i.e., current, voltage, and the measured impedance) and battery temperature, which can be expressed as,

$$\hat{T}_{avg} = NN\left(I, V_t, Z^*\right) \tag{5}$$

Finally, because it is not practical to perform the impedance measurement every second, the intermittently acquired impedance, along with the time-series current and voltage data, will be treated as the input to the neural network model to achieve real-time temperature estimation during online applications.

III. Experimental

In this section, both the experiments for obtaining classical EIS and operando impedance will be introduced. The tested battery is a 3.7V/50Ah NMC cell manufactured by CALB. The experimental setup for classical EIS measurement can be illustrated in Fig. 2(a), where an electrochemical workstation, a battery cycler, a thermal chamber, a temperature acquisition module, and a host computer are included. The battery cycler is used to adjust the cell SOC and the ambient temperature inside the thermal chamber can be changed to the set value. The electrochemical workstation is used to conduct the classical EIS measurement, during which galvanostatic mode is used and the peak-to-peak excitation current is 200 mA. The temperature

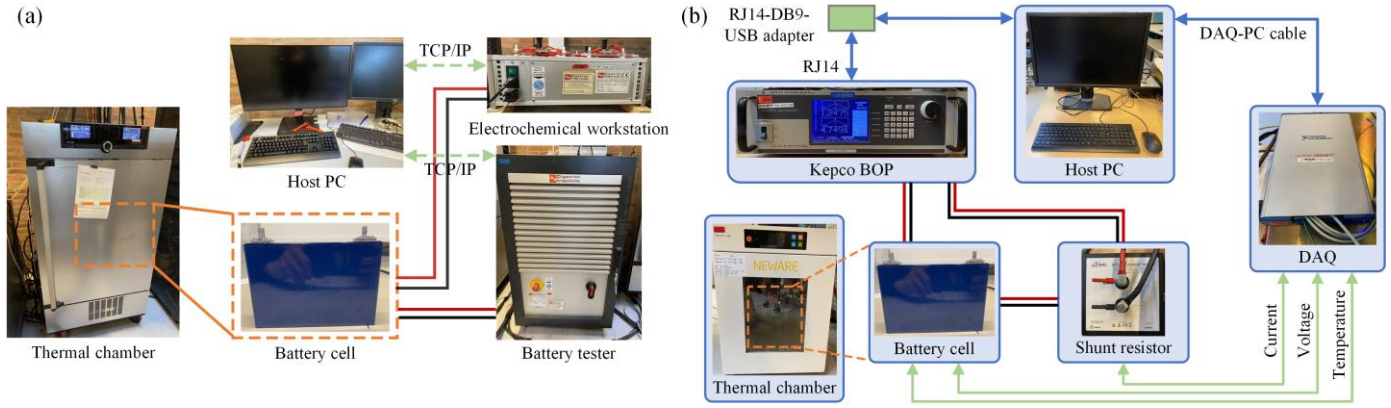

Fig. 2. Experimental setups for (a) classical EIS measurements and (b) operando impedance measurement.

TABLE I
BATTERY SPECIFICATIONS IN THE EIS DATASET

Cell Index	Cell Chemistry*	Format	Nominal Capacity	Manufacturer
# 1	NMC	Prismatic	50 Ah	CALB
# 2	NMC	Prismatic	50 Ah	N/A
# 3	NCA	Cylindrical	2.9 Ah	Panasonic
# 4	LFP	Prismatic	90 Ah	Thunder Sky
# 5	NCA	Cylindrical	4.8 Ah	Samsung

*NMC: Lithium Nickel Manganese Cobalt Oxide
NCA: Lithium Nickel Cobalt Aluminum Oxide
LFP: Lithium Iron Phosphate

TABLE II
DETAILS OF THE EIS DATASET USED IN THIS STUDY

Cell Index	Frequency range	Temperature	SOCs	Source
# 1	0.01 – 1157 Hz	15 ℃ - 45 ℃ with 5 ℃ interval	10% - 90% with 20% interval	Lab test
# 2	0.005 – 1584 Hz	−10 ℃ - 45 ℃ with 5 ℃ interval	10% - 90% with 20% interval	[44]
# 3	0.1 – 6000 Hz	−20 ℃, −10 ℃, 0 ℃, 10 ℃, 25 ℃	5% - 100% with 5% interval	[45]
# 4	10 – 5000 Hz	−20 ℃, −10 ℃, 10 ℃, 30 ℃, 50 ℃	0 - 100% with 20% interval	[33]
# 5	0.05 – 80 Hz	5 ℃, 25 ℃	10% - 90% with 10% interval (classical EIS) 0 – 78% with 1000 points (operando EIS)	[28]

acquisition module helps monitor the battery temperature during the test, and a K-type thermocouple placed at the center of the cell surface is connected to this module. The classical EIS measurements were conducted over a temperature range of 15 ℃ - 45 ℃ in intervals of 5 ℃, and over a range of 10% - 90% SOC in intervals of 20% (which covers the typical SOC usage range of many EVs). In demanding applications where batteries experience fully charging and fully discharging, smaller SOC intervals and a wider SOC range should be considered during the EIS measurement. The testing frequency ranges from 0.01 Hz to 6400 Hz. It should be noted that before each EIS measurement, the tested cell will rest for 1 h to reach both electrical and thermal equilibriums.

The collected classical EIS data is used for analysis and optimal impedance parameter selection. To parameterize and validate the proposed temperature estimation model, operando impedance data will also be collected, with the experimental setup shown in Fig. 2(b), where a current shunt, a bi-directional power supply from Kepco (Model BOP 10-75MG/ME), a data acquisition (DAQ) module from National Instruments, a thermal chamber, a host computer are involved. The bi-directional power supply is able to provide high-frequency current pulses up to 1000 Hz and be controlled by the host computer. The DAQ can provide the reference current profile to the power supply, and also record the voltages across the tested cell, the current shunt as well as the temperature measured by a K-type thermocouple placed at the cell surface. The tested cell is placed in the thermal chamber and thermally insulated during dynamic operations. This thermal boundary condition is created on purpose to minimize the internal temperature gradient so that the volume-averaged temperature of the cell is close to the surface temperature, which helps the validation of the methodology. To obtain the operando impedance, current pulses with the optimal excitation frequency f^* will be generated by the power supply and injected periodically during the cell operation.

IV. EIS DATA ANALYSIS AND OPTIMAL IMPEDANCE PARAMETER SELECTION

For impedance-based temperature estimation, it is important to select optimal impedance parameters to yield satisfactory estimation performance. Until now, there has been no consensus on which impedance parameters are the best for temperature estimation. In particular, batteries with different chemistries and formats exhibit different impedance characteristics regarding the shape of EIS as well as its dependence on SOC and temperature. As a result, it is difficult for the conclusion drawn based on one type of battery to be generalized to other batteries. In light of this, we aim to find a common characteristic of optimal impedance parameters from different cells used for temperature estimation. In this way, such parameters can be selected merely based on one EIS spectrum rather than a whole EIS dataset, which greatly reduces the need for a large number of EIS tests.

In this work, we not only collect the classical EIS data of the cell used in our lab test but also the EIS data of different batteries from the existing literature. The battery specifications of the collected EIS dataset can be summarized in Table I, which covers different cell chemistries, formats, and capacities. The details of these EIS datasets are provided in Table II, where each dataset contains the battery EIS at different temperatures and SOCs.

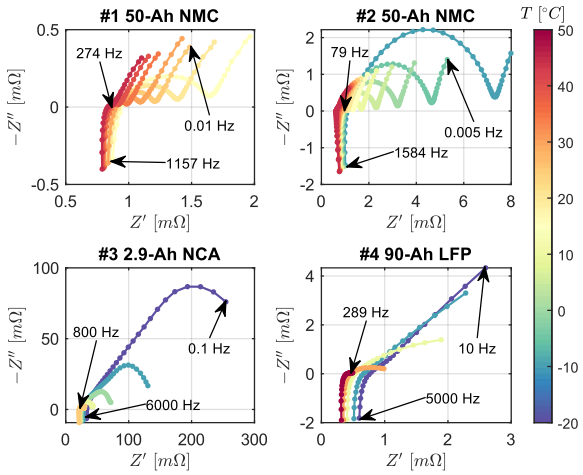

Fig. 3. Nyquist plot of EIS for cells #1-4 under different temperatures when SOC is constant.

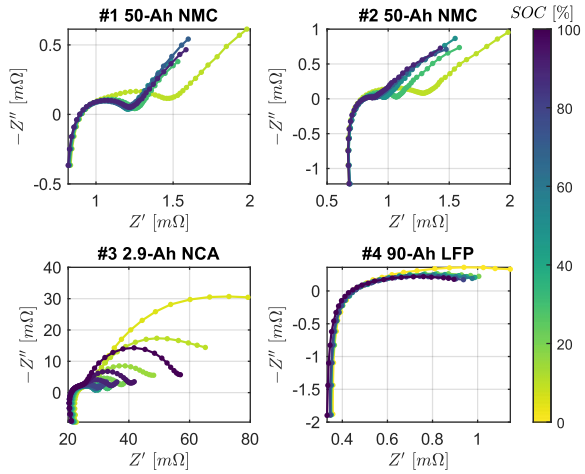

Fig. 4. Nyquist plot of EIS for cells #1-4 under different SOCs when the cell temperature is constant.

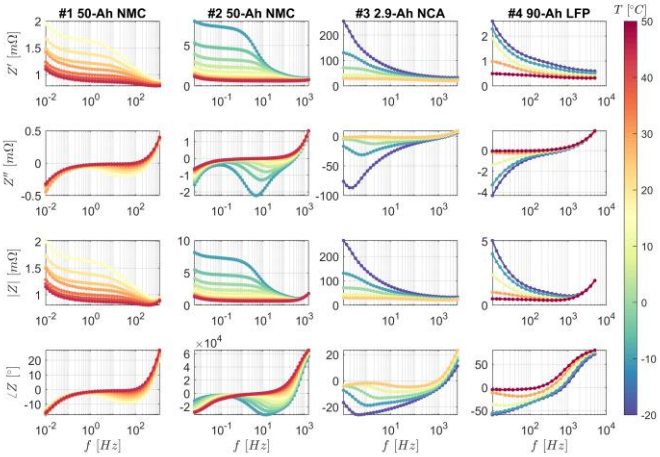

(a)

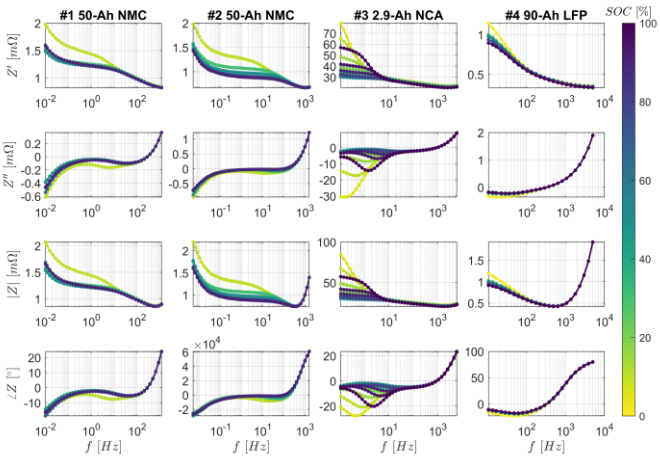

(b)

Fig. 5. Impedance parameters of cells #1-4 in the frequency domain. (a) Impedance parameters at different temperatures when SOC is kept constant, (b) Impedance parameter at different SOCs when temperature is kept constant.

TABLE III
CHARACTERISTIC FREQUENCIES OF THE EIS FOR CELL #1-4 AT AROUND ROOM TEMPERATURE AND 50% SOC

Cell index	f_{min} (Hz)	f at local minimum (Hz)	f at local maximum (Hz)	intercept f (Hz)	f_{max} (Hz)
# 1	0.01	2	37	274	1157
# 2	0.005	6	25	79	1854
# 3	0.1	1	34	800	6000
# 4	10	N/A	28	289	5000

A. Classical EIS data analysis

The EIS data from cells #1-4 will be used to analyze the temperature and SOC dependence of the impedance and select the optimal parameters based on the analysis. The Nyquist plots of these four batteries' EIS under different temperatures and SOCs are illustrated in Fig. 3 and Fig. 4, respectively. In Fig. 3, the lowest frequency, the intercept frequency, and the highest frequency at 25 ℃ are marked in the Nyquist plot. Apart from these three characteristic frequencies, the frequency with local minimum (between the low-frequency range and medium-frequency range), as well as the frequency with local maximum (which occurs on the semi-circle in the mid-high frequency range) at 25 ℃ have also been identified. These characteristic frequencies can be summarized in Table III. It can be seen from both Fig. 3 and Table III that although the EIS shapes of different batteries are similar, their characteristics vary greatly. In particular, the intercept frequency and the frequency where the local maximum occurs are quite different, even for cells #1 and #2 which have the same chemistry, format, and capacity. In addition, for these four cells, the SOC affects the EIS to different extents in the Nyquist plot, as shown in Fig. 4. The effect of SOC on battery EIS is most insignificant in cell #4 while most significant in cell #3. In cell #3, the impedance increases significantly at both low and high SOC ranges, and decreases when the SOC is in the middle range. As for two 50-Ah NMC cells, the impedance only increases significantly at a low SOC range, with notable impedance shift when SOC is less than 30% for cell #1 and when SOC is less than 50% for cell #2.

Owing to the different EIS characteristics of different cells, the impedance parameters must be analyzed in the frequency domain regarding their temperature and SOC dependence so as to select the optimal impedance parameters. All the impedance parameters of cells #1-4, including Z', Z'', $|Z|$, and $\angle Z$, are plotted against the frequency in a semi-logarithmic graph, as illustrated in Fig. 5. It can be seen from Fig. 5 that different impedance parameters exhibit different dependencies on

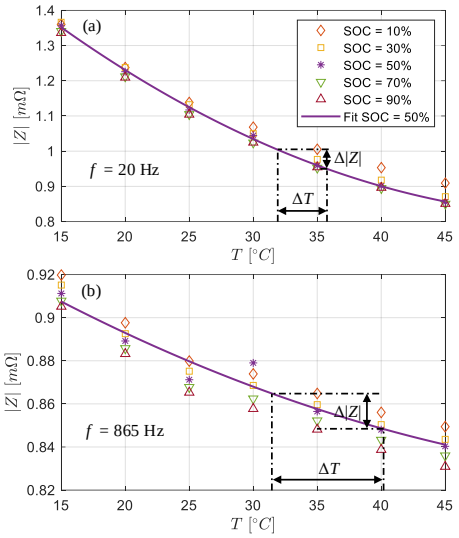

Fig. 6. Temperature estimation errors caused by impedance variation due to SOC uncertainties.

battery temperature and SOC. In Fig. 5(a), the real part and magnitude of these four cells show significant variation against temperature in a wide frequency range, especially at low frequencies. With the increase in frequency, the sensitivity of these two impedance parameters to temperature decreases gradually. As for the imaginary part and the phase, they are sensitive to the temperature in the whole frequency range in cell #3 and cell #4, with a decrease in sensitivity when frequency increases. Nevertheless, in cell #1 and cell #2, these two impedance parameters are only highly sensitive to temperature in specific frequency ranges, like 10-500 Hz for the phase in cell #1 and 1-200 Hz for the imaginary part in cell #2.

Apart from the temperature dependence, it is also important to examine the SOC dependence of impedance parameters to avoid the SOC uncertainties on the temperature estimation. It can be shown in Fig. 5(b) that the variation of all the impedance parameters induced by SOC basically occurs at low frequencies, though the specific frequency range varies from cell to cell. At high frequencies, the impedance parameters under different SOCs tend to converge so that the effect of SOC on impedance parameters becomes small. For cell #1, both the real part and magnitude start to converge at about 20 Hz, while the imaginary part and phase start to converge at about 50 Hz. Despite the same chemistry, format, and capacity, the SOC dependence of impedance parameters in cell #2 is quite different from that in cell #1. In cell #2, only the real part and the magnitude of the impedance are notably affected by the SOC change when the frequency is less than 100 Hz, while the imaginary part and the phase do not change significantly with SOC in the whole frequency range. In cell #3, the SOC-insensitive frequency range is above 6 Hz for real part and magnitude, and above 33 Hz for imaginary part and phase. In cell #4, the effect of SOC becomes insignificant at the frequency range above 100 Hz for all the impedance parameters.

From the above analysis, it can be concluded that different impedance parameters usually exhibit different sensitivities to temperature and SOC under different frequencies. Such characteristics may vary from cell to cell, even for the cells with the same cell chemistry and format, which explains distinct

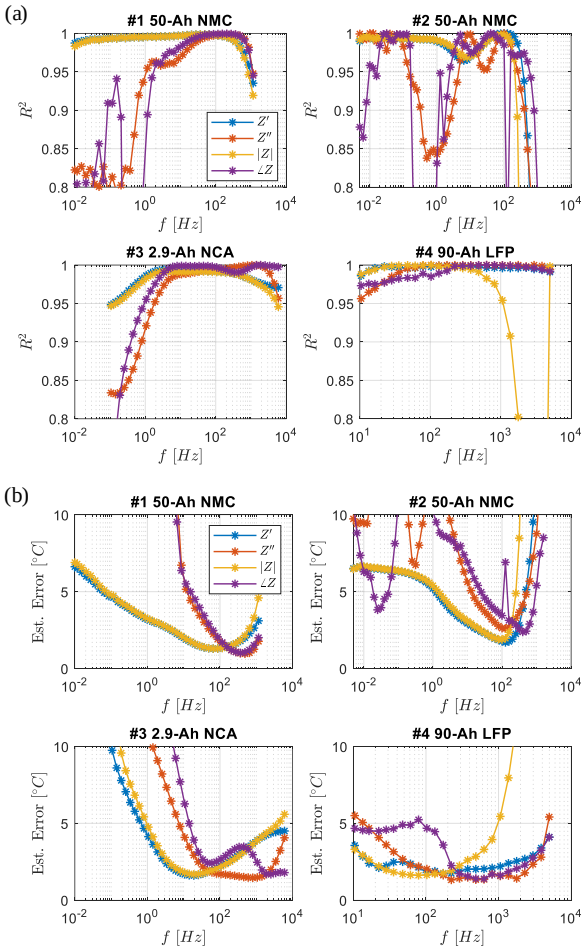

Fig. 7. (a) R^2 of the fitting at different frequencies, (b) RMSE of the fitting results at different frequencies.

conclusions for selecting optimal impedance parameters for temperature estimation in the existing literature [6], [19], [20].

B. Optimal impedance parameter selection

Selecting a temperature-sensitive impedance parameter and an excitation frequency is of great importance to constructing the estimation model, where the negative effect of SOC uncertainties should also be minimized. As such, both the temperature and SOC dependence of these impedance parameters should be considered during the selection process. As a general trend according to the EIS data analysis, the variation of battery impedance against SOC will diminish with the increase of excitation frequency. Nevertheless, merely selecting the impedance parameters in the high-frequency region does not contribute to better temperature estimation performance due to the reduced sensitivity of impedance to battery temperature. As a result, a small variation of impedance caused by SOC uncertainties will lead to a large estimation error in temperature, as discussed in Ref. [32]. In this work, we illustrate this issue in Fig. 6 using $|Z|$ at different frequencies (i.e., 20 Hz and 865 Hz) as an example. At 20 Hz, the high sensitivity of $|Z|$ to temperature causes a larger slop of the fitting function and therefore the $|Z|$ variation brought by SOC uncertainties causes a temperature estimation uncertainty ΔT of less than 5 °C. At 865 Hz, however, the reduced temperature

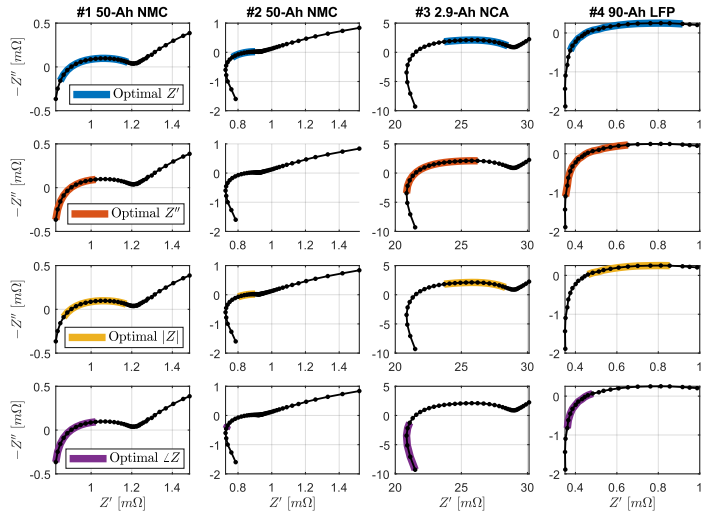

Fig. 8. Location of optimal impedance parameters used for temperature estimation in the Nyquist plot. Blue, orange, yellow, and purple lines indicate the locations of the optimal real part, imaginary part, magnitude, and phase in the impedance spectrum respectively.

sensitivity of $|Z|$ yields a much smaller slop of the fitting function, and $|Z|$ variation will make ΔT nearly up to 10 ℃. Hence, the optimal impedance parameter selection should balance the parameters' sensitivity to both temperature and SOC to yield good estimation performance.

Different from the sensitivity analysis of battery impedance in the literature [33], this paper adopts another method to select optimal impedance parameters. The impedance-temperature relationship will be fitted with a second-order polynomial at each frequency using the impedance data at 50% SOC (40% SOC for cell #4) [22],

$$\theta = a_1 + a_2 T_{avg} + a_3 T_{avg}^2 \tag{6}$$

where θ is the impedance parameter and can be Z', Z'', $|Z|$, or $\angle Z$, a_1, a_2, and a_3 are the constant coefficients. Then the temperature of the cell can be obtained via the inverse function of Eq. (6). To quantify the effect of SOC uncertainties on the estimation performance, the impedance data with the same frequency but different SOCs will be used to evaluate the estimation performance, and the RMSE is adopted,

$$RMSE = \sqrt{\frac{1}{N}\sum_{k=1}^{N}\left(\hat{T}_{avg,k} - T_{avg,k}\right)^2} \tag{7}$$

In the meantime, the R-squared of the fitting at 50% SOC will also be calculated as the goodness of fit (GOF) to evaluate whether the impedance parameters follow a monotonic change with battery temperature. The R-squared can be calculated as,

$$R^2 = 1 - \frac{RSS}{TSS} = 1 - \frac{\sum\left(\hat{T}_{avg,k} - T_{avg,k}\right)^2}{\sum\left(T_{avg,k} - \bar{T}_{avg}\right)^2} \tag{8}$$

where RSS is the sum of squares of residuals, TSS is the total sum of squares, and higher R^2 indicates better GOF.

The R^2 of the fitting and the RMSE of the estimation using different impedance parameters and frequencies can be illustrated in Fig. 7(a) and (b), respectively. It can be seen from the results that different impedance parameters only show high GOF in specific frequency ranges, with R^2 above 0.95. The fitting using Z' and $|Z|$ shows higher R^2 than using other parameters in a wider frequency range. Lower RMSE indicates higher robustness of the estimation since it is less likely affected by the SOC uncertainties. It can be seen from Fig. 7 that higher R^2 often contribute to lower RMSE. In Fig. 7(b), there exists an optimal frequency range for different impedance parameters that enables accurate and robust estimation. Z' and $|Z|$ share similar characteristics while Z'' and $\angle Z$ share similar trend. Furthermore, the optimal frequency range for Z' and $|Z|$ are lower that using Z'' and $\angle Z$, which suggests that the estimation using Z' and $|Z|$ are easier to be implemented in real-world applications owing to lower demand on excitation frequencies.

To select the optimal impedance parameters for temperature estimation, we set a threshold (2.5 ℃ in this work) in Fig. 7(b) to find the frequencies under which the RMSE is below this threshold. The corresponding impedance parameter under such frequencies is regarded as the optimal impedance parameter which is able to yield accurate and robust temperature estimation. Since the frequency characteristics of different batteries are different, merely presenting the optimal frequencies for different impedance parameters cannot reveal their common characteristics, which explains different conclusions in the literature in terms of optimal impedance parameters [6], [20]. Therefore, we attempt to highlight the location of these optimal impedance parameters in the Nyquist plot to find the common feature of these parameters in a typical impedance spectrum at 25 ℃ and 50% SOC.

Fig. 8 illustrates the location of optimal impedance parameters of four studied batteries in the Nyquist plot, where different colors represent different optimal impedance parameters. As for four impedance parameters, including Z', Z'', $|Z|$, and $\angle Z$, there exist different optimal frequency ranges (i.e., different locations in the Nyquist plot) that contribute to better temperature estimation performance. Generally, optimal Z' and $|Z|$ have quite similar locations in Nyquist plot, while optimal Z'' and $\angle Z$ have similar locations. All these four parameters lie in the mid- and high-frequency regions of the spectrum, which represent the processes such as

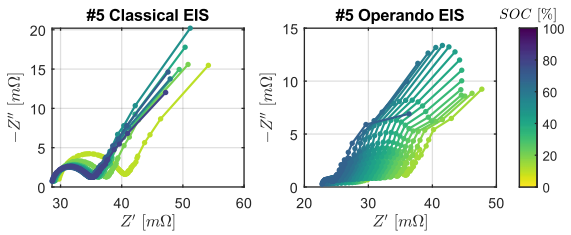

Fig. 9. Classical EIS and operando EIS from cell #5 at different SOCs.

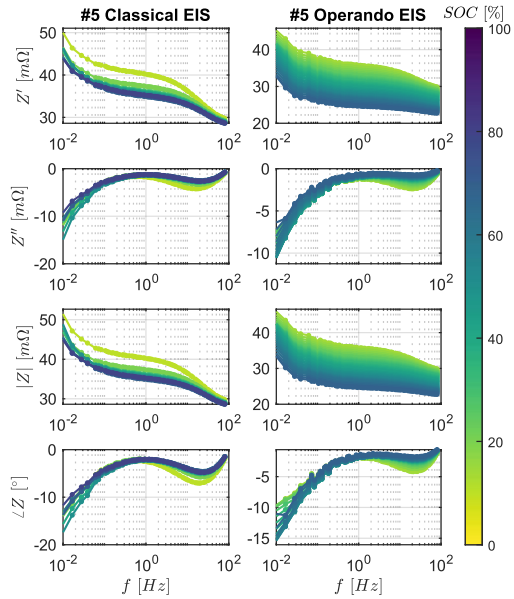

Fig. 10. Classical EIS and operando EIS in the frequency domain.

charge transfer, solid electrolyte interphase (SEI), ohmic resistance, and induction. It can also be found in Fig. 8 that the location of the same impedance parameter in different batteries' EIS has the same feature. The location of optimal Z' and $|Z|$ in the EIS of all the batteries contains the low-frequency part of the semi-circle (i.e., charge transfer process). In some cells (e.g., cell #1 and cell #4), the high-frequency semi-circle, ohmic resistance, and induction part are also included. As for optimal Z'' and $\angle Z$, they basically lie on the high-frequency semi-circle (i.e., SEI), ohmic resistance, and some induction part. Therefore, the impedance on the semi-circle of the EIS spectrum can often be a reliable choice regardless of battery type when selecting impedance parameters. If $\angle Z$ is to be used, the impedance at the induction part is the preferred choice. This conclusion also coincides with the findings in the existing literature [26], [32], [34], where the SOC-independent process related to SEI is regarded as the contributor to impedance-based temperature estimation.

Knowing the common characteristics of these optimal impedance parameters can greatly facilitate the optimal parameter selection for battery temperature estimation. Previously, the EIS dataset of the target battery at different SOCs and temperatures has to be collected and the EIS analysis needs to be performed to find suitable parameters. For different target batteries, the aforementioned procedures have to be conducted repeatedly, which takes a significant amount of time. Now, with this generalized rule, optimal impedance parameters can be picked easily merely from one EIS spectrum of the cell efficiently.

C. Classical impedance vs operando impedance

Normally, the classical EIS of a battery is measured after sufficient relaxation, when the cell is under a steady state. However, in real-world applications, it is impractical to interrupt the battery operations to perform classical EIS measurements to acquire timely impedance information. In this regard, the EIS must be measured without affecting the battery operations, but the online obtained operando EIS is usually beyond linearity and stationarity, which makes it different from the classical one [28], [29].

To ensure that the optimal impedance selection conclusion from the classical EIS analysis can be applied to online applications, the classical EIS and operando EIS must be compared to ensure that both impedances exhibit similar SOC dependence. To this end, the EIS dataset from cell #5 is used for comparison, as illustrated in Fig. 9, which contains both the classical EIS and operando EIS at nearly the same temperature but different SOCs. The operando EIS is obtained when the battery is subject to a charging current of 2.4 A from a fully discharged state. The temperature of the cell rises at the beginning of charging but becomes stable from about 15% SOC [28].

Fig. 9 suggests that the operando EIS is different from the classical one in terms of magnitude despite their similar shape. Both the real part and imaginary part of the operando impedance are smaller than the classical one, as also pointed out by ref. [29]. As SOC increases, both EISs shrink towards the origin, exhibiting a similar trend on SOC. To further examine the SOC dependence of all the impedance parameters, they are plotted in the frequency domain in a semi-logarithmic graph, as illustrated in Fig. 10. The results indicate that Z'' and $\angle Z$ have a highly similar dependence on battery SOC as their shape are quite similar. As for Z' and $|Z|$, both classical impedance and operando impedance tend to converge as the frequency becomes higher. The classical impedance converges well at the high-frequency region while the operando one will still be affected by SOC uncertainties in the same region. Nevertheless, despite some discrepancies, it is fair to say that all the impedance parameters in the classical EIS and operando EIS exhibit highly similar trends. Therefore, it is reasonable to apply the optimal impedance parameters selected from the classical EIS to online applications.

V. Temperature Estimation Via Online Impedance Acquisition

With the optimal impedance parameters selected, the single-frequency impedance needs to be measured online during battery operations for temperature estimation. This section introduces an online impedance acquisition method using pulse current injection and a neural network model to achieve real-time sensorless temperature estimation.

A. Online impedance acquisition

Existing impedance-based temperature estimation methods are developed and validated based on the impedance which is measured after a sufficient relaxation. In real-world

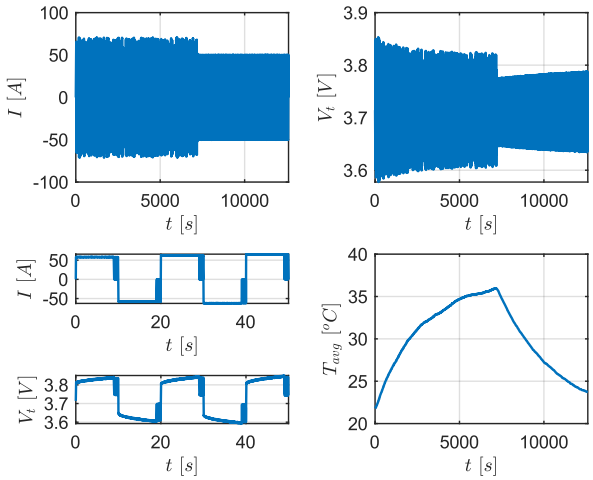

Fig. 11. Current, voltage, temperature of the cell #1 under random BPC with pulse current injection.

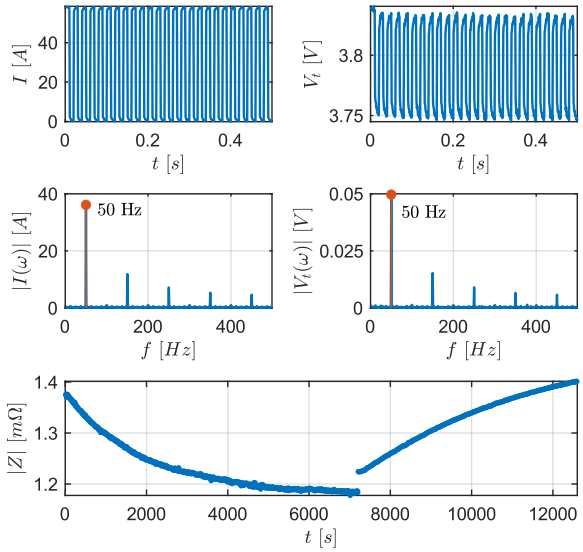

Fig. 12. Measured current and voltage during one pulse injection period for operando impedance extraction, plotted in both time and frequency domains, as well as the extracted impedance in the whole testing cycle.

applications, however, it is difficult to guarantee such measurement conditions, which brings challenges to real-time monitoring of battery temperature especially under dynamic operations. In addition, there is no guarantee that the harmonics at the frequency of f^* will always exist under dynamic profiles, and therefore the required excitation signals for impedance extraction should be created artificially. Despite extensive studies on the fast acquisition of battery impedance via various specifically designed excitations, obtaining battery impedance under dynamic conditions is still lacking [27], [35], [36]. Some attempts have been made to superimpose the small disturbance on the operating current, but the signal-to-noise ratio (SNR) cannot be guaranteed under dynamic current conditions where the current might vary significantly [29], [37].

In light of this, we propose a novel method to measure the operando impedance during operations through pulse current injection. Under load conditions, the pulse current can be generated by interrupting the cell operations at a frequency f^* within a very short period (e.g., 1 s or 0.5 s). In this way, the battery is switched between the active and interrupted modes at the frequency f^* during this short period so that the normal battery operation will not be affected. The load current itself can be the excitation source for the impedance measurement and the pulse amplitude is equal to the load current. When the battery is under rest conditions, a short-period bi-directional pulse current at the frequency of f^* can be generated by an external excitation source and injected into the cell for impedance measurement. In this way, the pulse current can be injected intermittently under both the load and rest conditions during battery operations to extract impedance information while the SNR can also be guaranteed. FFT can be applied to the current and voltage signals during the pulse injection period to extract the harmonic component just at the frequency f^*. Then operando impedance parameters at f^* can be calculated accordingly and used for temperature estimation.

The pulse current can be generated more easily at the cell level in a reconfigurable battery system where each cell can be kept in active or bypass mode by controlling the switches in the system, as described in ref. [38], [39], [40]. By switching between the active and bypass modes at a desired frequency, pulse currents can be generated independently within each cell without affecting the overall performance of the battery system [40]. In a broader context, such actively generated pulse current can increase the "richness" of the excitation signal and contribute to better state and parameter estimations [41].

To demonstrate the proposed online impedance acquisition method, a dynamic test conducted on cell #1 with random bi-directional pulse currents (BPC) at 0.05 Hz based on the experimental setup in Fig. 2(b) is presented here. The collected experimental data is illustrated in Fig. 11, including the current, voltage, and cell temperature. The sampling frequency during this test is kept at 1 kHz and the measured temperature is smoothed by Gaussian weighted average with a window size of 20 s. The amplitude of the pulse current in each period varies randomly between 1C and 1.5C, and the SOC of the cell remains stable at around 50%. The pulse current injection occurs periodically every 10 s (i.e., the last 1 s of each half period of BPC) with a switching frequency of 50 Hz. The temperature increase of the cell is nearly 15 ℃ at the end of the random BPC due to thermal insulation. Then the cell has a 2-h rest phase, during which a 1-s bi-directional pulse current injection with the amplitude of 1C occurs every 20 s to extract the battery impedance timely.

Details of the pulse current injection as well as the impedance extraction are shown in Fig. 12. The current and voltage during the first 0.5 s of the pulse injection period under load conditions are first illustrated. As the cell is switched between active and interrupted mode, the generated pulse current varies in an "on-off" pattern at a frequency f^*. The FFT results of the current and voltage during this 1-s period are also shown. Although there are other harmonic components at 150 Hz, 250 Hz, 350 Hz, and 450 Hz due to the 1-kHz sampling frequency, only the 50-Hz component is needed to capture the selected impedance. It can be seen from the extracted

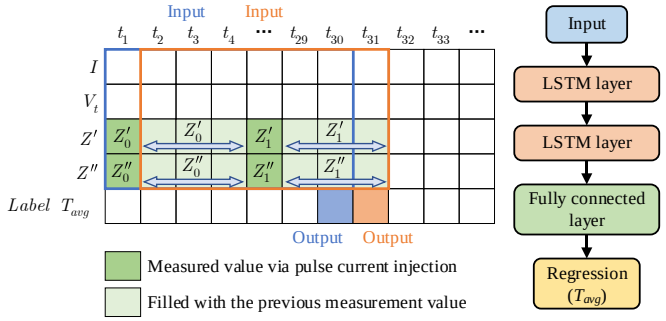

Fig. 13. Framework for real-time sensorless temperature estimation based on LSTM-RNN.

impedance that as the battery temperature increases, $|Z|$ decreases accordingly. During the rest phase, $|Z|$ increases as the battery temperature drops. There is a jump in the calculated impedance at the beginning of the rest phase, which is assumed to be caused by different excitation manner (i.e., unidirectional pulse current and bidirectional pulse current for load and rest phase respectively). Therefore, the extracted operando impedance exhibits quite a good dependence on battery temperature.

It should be noted that the computational efficiency of FFT can be further improved by designing the length of pulse current injection or the sampling frequency to facilitate online implementation. For instance, the sampling frequency does not necessarily have to be high since only the harmonic component at the frequency f^* is needed.

B. Real-time sensorless temperature estimation

The single-frequency operando impedance extracted through pulse current injection can be used as an indicator of the battery volume-average temperature [22], [23]. However, there are two challenges for real-time temperature estimation based on the operando impedance: (1) The impedance acquisition through pulse current injection cannot be performed every second but might be every 10 or 20 s, making it difficult to track the battery temperature between two impedance acquisitions. (2) The operando impedance obtained under large current excitations not only depends on battery temperature but also on the current and usage history [28].

To overcome the aforementioned two challenges, a data-driven estimation framework based on LSTM-RNN is proposed, as shown in Fig.13. Time-series data in a 30-s sliding window, which contains battery current, voltage, as well as the real part and imaginary part of the impedance, is fed into the LSTM-RNN as input. The missing impedance data between two adjacent measurements is filled with the one from the previous measurement. Before being inputted to the neural network, the data has been normalized between [0,1] to reduce the magnitude differences between input features. The battery temperature at the last time index in the sliding window is set as the output. The LSTM-RNN model consists of two LSTM layers with 50 hidden nodes in each layer, and a fully connected layer with one neuron as the regression output. Dropout with a probability of 0.2 is added after each LSTM layer to increase the model generalization ability and prevent overfitting. To avoid the estimation variation brought by impedance measurement noise, a filter (i.e., Gaussian weighted average with a window size of 120 s) can be added after the LSTM-RNN output to smooth the estimation results. The maximum training epoch is set as 150 and Adam optimization is used during the training process.

TABLE IV
SUMMARY OF BATTERIES AND TESTING PROFILES FOR VALIDATION

Cell Index	Cell information	f^* / Hz	Ambient	Training set	Testing set
# 1	50-Ah prismatic NMC fresh cell (CALB)	50	20 ℃	Random BPC, 1.2-C BPC	1-C BPC
# 6	2.2-Ah 18650 cylindrical NMC fresh cell (HAIDI)	10	25 ℃	Random BPC, 2-C BPC, HEV-1	1.5-C BPC, HEV-2
# 7	2.2-Ah 18650 cylindrical NMC aged cell (HAIDI)	10	20 ℃	FUDS	WLTP
# 8	2.3-Ah 26650 cylindrical LFP aged cell (A123)	50	25 ℃	FUDS	WLTP

TABLE V
PERFORMANCE OF THE PROPOSED LSTM-RNN MODEL IN DIFFERENT BATTERIES AND OPERATING CONDITIONS

Cell index	Testing cycle	Ambient / ℃	Error metrics		
			RMSE (℃)	MAE (℃)	MAX (℃)
# 1	1-C BPC	20 ℃	0.20	0.17	0.56
# 6	1.5-C BPC	25 ℃	0.35	0.27	0.96
	HEV-2	25 ℃	0.22	0.16	1.08
# 7	WLTP	20 ℃	0.39	0.33	1.00
# 8	WLTP	25 ℃	0.46	0.42	1.84

The proposed methodology is validated against four different batteries as well as various current profiles. The information and the testing profiles of these four batteries can be summarized in Table IV, where the cells differ in chemistry, formats, aging status, and manufacturers. Except for cell #1, there is no complete EIS dataset for cells #6-8 used for impedance parameter selection. Instead, the optimal impedance is selected merely based on one EIS spectrum according to the selection rule discussed in the previous section. The impedance that lies on the low-frequency part of the semi-circle on the EIS spectrum is selected, and therefore different f^* is used for different cells. In addition, dynamic current profiles, including BPCs, hybrid electric vehicle (HEV) driving cycles, federal urban driving schedule (FUDS), and worldwide harmonized light vehicles test procedure (WLTP), are involved in the validation dataset. Instead of training a model that covers all the cells and operating scenarios, separate models are developed for each cell. To evaluate the estimation performance, other metrics such as mean absolute error (MAE) and maximum error (MAX) are also used.

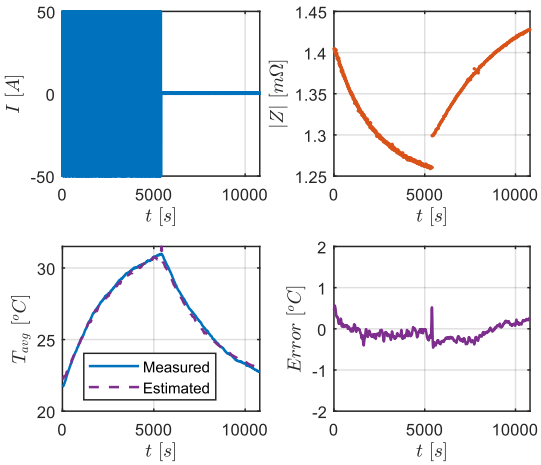

Fig. 14. Current, magnitude of the operando impedance, estimation results of the cell temperature, and estimation errors of cell #1 under 1-C BPC.

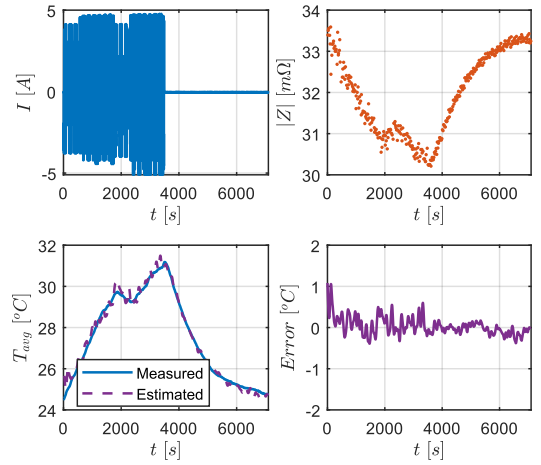

Fig. 15. Current, magnitude of the operando impedance, estimation results of the cell temperature, and estimation errors of cell #6 under HEV-2.

The estimation performance of the proposed framework in these four testing cells is summarized in Table V. The RMSE and MAE of all the estimations are within 0.5 ℃, and the MAX are within 1.1 ℃ in most cases (less than 2 ℃ in worst case), demonstrating high accuracy of the LSTM-RNN estimation models and the effectiveness of the proposed method in different batteries and operating conditions. Three representative cases, including the 1-C BPC cycle of cell #1, the HEV-2 cycle of cell #6, and the WLTP cycle of cell #8, are presented in Figs. 14-16, respectively. The current, the magnitude of the measured operando impedance (as it is a combination of the real part and the imaginary part), as well as the estimation results and errors, have been shown in each figure. In these three cases, both the current and the temperature are illustrated with a sampling frequency of 1 Hz. It can be seen from these three cases that the measured impedance at f^* shows a clear and opposite variation trend with battery temperature. That is, the impedance magnitude decreases with the battery temperature rise and increases when the battery cools down. It is interesting that the operando impedance trajectory exhibits a highly similar but opposite shape to the

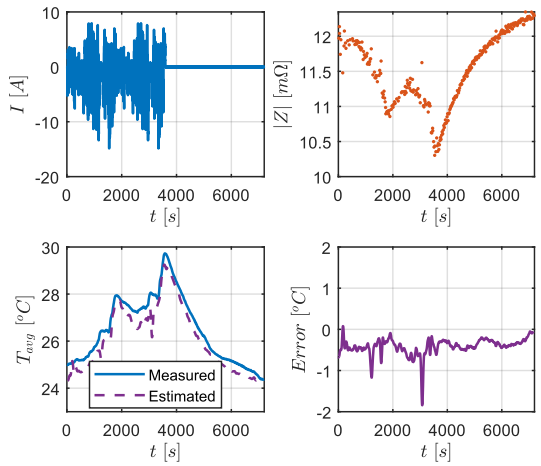

Fig. 16. Current, magnitude of the operando impedance, estimation results of the cell temperature, and estimation errors of cell #8 under WLTP.

temperature curve, indicating the high correlation between the selected impedance and the battery temperature. Nevertheless, the trajectory of the measured operando impedance might not be very smooth, particularly under dynamic current conditions like HEV-2 and WLTP cycles, which could be caused by different pulse excitations. Despite this, the measured operando impedance can still be a good input feature of the LSTM-RNN model to achieve accurate estimation as it is high temperature-sensitive and SOC-insensitive. The estimation errors in these three presented scenarios are within ±1 ℃ most of the time, and therefore the proposed method is able to provide effective monitoring of battery SOT.

C. Methodology comparison and robustness test

The superiority of the proposed method can be further demonstrated by comparing it with traditional sensorless temperature estimation techniques. The comparison results are illustrated in Fig. 17 and summarized in Table VI. Nine typical techniques, including classical impedance-based, operando impedance-based, lumped-mass thermal model-based, empirical model-based, and pure data-driven model, have been compared using the testing cycles of cell #1. For both operando and classical impedance-based estimations, the corresponding impedance parameter will be inputted to a following second-order polynomial estimation function,

$$T_{avg} = a_1 + a_2\theta + a_3\theta^2 \tag{9}$$

In thermal model-based estimations, the lumped-mass thermal model is adopted with the ambient temperature and the heat generation as input [42], [43]. In empirical models, the following empirical equation will be used, and the temperature can be calculated in an iterative way.

$$T_{avg,k+1} = aT_{avg,k} + b\left(I_k\right)^2 + c \tag{10}$$

The aforementioned two types of models often require to be well parameterized in order to achieve high estimation performance. Both inaccurate model initialization and model parameter uncertainties will lead to inferior model performance. Therefore, in this paper, we change the heat transfer coefficient in the lumped-mass thermal model to be 100% higher to create model parameter uncertainties, while the other model parameters remain unchanged. A bias of 5 ℃ is added to the

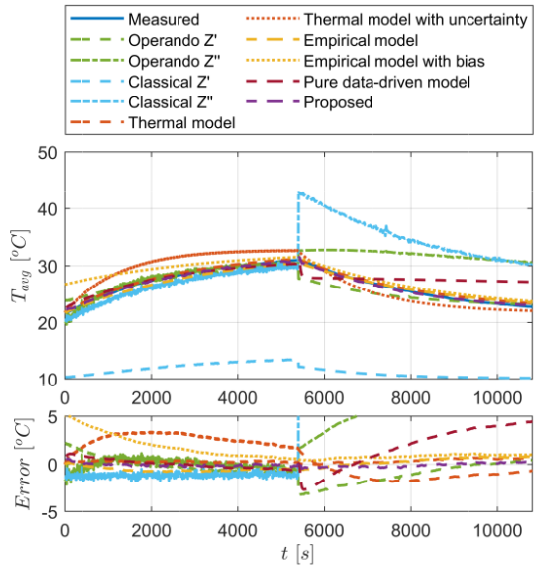

Fig. 17. Comparison of different sensorless temperature estimation methods under 1-C BPC of cell #1.

TABLE VI
COMPARISON OF DIFFERENT SENSORLESS TEMPERATURE ESTIMATION METHOD UNDER 1-C BPC OF CELL #1

Estimation Method	Error metrics		
	RMSE (°C)	MAE (°C)	MAX (°C)
Operando Z'(2^{nd}-order polynomial)	1.11	0.85	3.25
Operando Z''(2^{nd}-order polynomial)	3.69	2.3	7.94
Classical Z' (2^{nd}-order polynomial)	15.54	15.44	18.82
Classical Z'' (2^{nd}-order polynomial)	5.44	3.82	11.92
Lumped-mass thermal model (well-parameterized)	0.35	0.31	0.65
Lumped-mass thermal model (with parameter uncertainty)	2.07	1.88	3.35
Empirical model (well-parameterized)	0.55	0.5	0.8
Empirical model (with initialization bias)	1.74	1.37	5.04
Pure data-driven model	1.99	1.41	4.45
Proposed method	0.20	0.17	0.56

initialization in the empirical model to create inaccurate initializations. In the pure data-driven model, only the 30-second current and voltage data are used as input to the LSTM-RNN, which has the same structure as shown in Fig. 13. All these nine methods are first parameterized/trained with the random BPC cycle and EIS data of cell #1 and tested with 1-C BPC cycle.

It can be seen from Fig. 17 that classical impedance-based methods have the worst performance. The difference between the classical impedance and operando impedance as well as the change of cell connection resistance are assumed to be the root cause of such performances. Operando impedance-based techniques, though with a higher accuracy, still cannot achieve high-performance estimation. The reason is that the dependence of impedance on excitation current and usage history is neglected by the second-order polynomial estimation function. In particular, the estimations based on operando impedance suffer from increased errors during the rest period. If well parameterized, both thermal model-based and empirical model-based estimation, are able to achieve satisfactory estimation accuracy. Nevertheless, the parameter and initialization errors, which are quite common in real-world

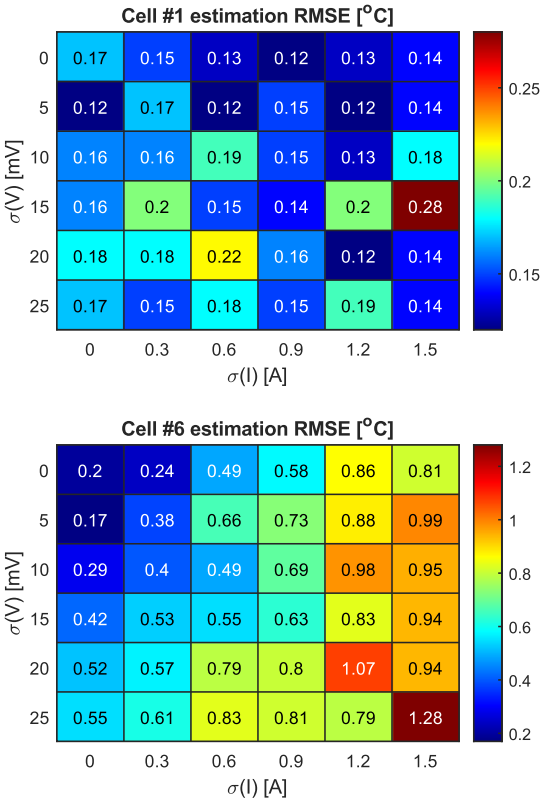

Fig. 18. Robustness test of the proposed method under 1-C BPC (cell #1) and HEV-2 (cell #6) cycle with different current and voltage measurement noise.

applications, will cause significant degradation in estimation performance. As for the pure data-driven estimation, since the battery voltage is not very sensitive to temperature change, the estimation performance is even worse than a poorly parameterized thermal model, as also pointed out by the ref. [42]. From this comparison, it can be seen that the proposed method is able to achieve much higher estimation accuracy than the existing techniques, owing to the nonlinear mapping capabilities of the LSTM-RNN model, temperature-sensitive input features (i.e., optimal impedance), and the consideration of current and usage history. Since the measured optimal impedance is determined by the battery temperature, it can be independent of the ambient and cooling conditions, making it possible for this method to work adaptively under different thermal boundary conditions.

Since the operando impedance is extracted from the current and voltage, the measurement noise will inevitably affect the accuracy of the acquired impedance and further influence the estimation performance. To this end, it is also important to examine the robustness of the proposed method against measurement noise. Zero-mean white Gaussian noises with different standard deviations are added to the original current and voltage data in both the training set and testing set, despite the presence of existing noise in the original data. The same LSTM-RNN model is used for this robustness test, but the dropout is not adopted here to ensure repeatable results.

The estimation results with different noise levels under 1-C BPC (cell #1) and HEV-2 (cell #6) are illustrated in Fig. 18. As can be seen from this heatmap, for large-format cells (i.e., cell

#1), the estimation can be robust to measurement noises as the studied noise level produce virtually no effect on the impedance calculation. The RMSEs are generally within 0.2 ℃ for the majority of cases. As for small-format cells (e.g., cell #6), however, the operating current is still small even at a higher rate so the impedance extraction can be quite susceptible to the measurement noise. Therefore, both the current and voltage noises bring significant errors to the estimation performance. Under the measurement noise in this study, the current noise has a much larger impact on the estimation performance than the voltage noise does. If the measurement noise can be maintained within a threshold (e.g., $\sigma(I)$ less than 0.6 A and $\sigma(V)$ less than 15 mV), the estimation accuracy can still be satisfactory.

VI. Conclusion and Future Work

Online sensorless monitoring of battery temperature plays an indispensable role in battery safety, performance, and reliability management given sparsely allocated onboard temperature sensors and their inability to sense internal temperature. This paper introduces a temperature estimation method to capture the volume-average temperature of batteries in real time with online operando impedance acquisition. The common characteristic of optimal impedance parameters for temperature estimation from different batteries has been uncovered through comprehensive EIS analysis. It was found that the optimal impedance lies on the semi-circle as well as some induction parts of the EIS spectrum, regardless of battery chemistries and formats. This generalized rule helps select the optimal impedance parameters efficiently just from one EIS spectrum, without the need to collect a large EIS dataset for the target cell like traditional methods do. Then, the selected impedance parameter can be measured online through 1-s active pulse current injection and FFT, even under highly dynamic operating conditions, and used as an indicator of battery temperature. Finally, a real-time temperature estimation framework based on LSTM-RNN is developed to achieve accurate and timely temperature estimation by taking advantage of the intermittently measured impedance, as well as time-series current and voltage data. The proposed operando impedance-based method has been validated against different batteries and working conditions, with RMSE less than 0.46 ℃.

The methodology in this study is developed without considering the effect of battery degradation, making it challenging to achieve effective temperature monitoring in the long term. In particular, with battery aging, the change in battery impedance will inevitably bring errors to the temperature estimation if the algorithm is not updated timely. Therefore, future work can be conducted to update the estimation algorithm periodically over time to account for the impedance change caused by aging. Alternatively, new impedance parameters that are sensitive to battery temperature while insensitive to both the SOC and aging can also be selected. In this way, the estimation can be adaptive to battery aging.

Acknowledgment

The authors would like to thank Professor Henk Jan Bergveld at Eindhoven University of Technology for sharing the EIS data of cell #4 in this work, and Minh Tran at Tampere University for his advice and help with the experimental setup for online impedance measurement.

References

[1] C. Xu *et al.*, "Electric vehicle batteries alone could satisfy short-term grid storage demand by as early as 2030," *Nat Commun*, vol. 14, no. 1, p. 119, Jan. 2023, doi: 10.1038/s41467-022-35393-0.

[2] V. Viswanathan *et al.*, "The challenges and opportunities of battery-powered flight," *Nature*, vol. 601, no. 7894. Nature Research, pp. 519–525, Jan. 27, 2022. doi: 10.1038/s41586-021-04139-1.

[3] M. Dubarry, N. Costa, and D. Matthews, "Data-driven direct diagnosis of Li-ion batteries connected to photovoltaics," *Nat Commun*, vol. 14, no. 1, p. 3138, May 2023, doi: 10.1038/s41467-023-38895-7.

[4] J. S. Edge *et al.*, "Lithium ion battery degradation: what you need to know," *Physical Chemistry Chemical Physics*, vol. 23, no. 14. pp. 8200–8221, 2021. doi: 10.1039/d1cp00359c.

[5] X. Feng, M. Ouyang, X. Liu, L. Lu, Y. Xia, and X. He, "Thermal runaway mechanism of lithium ion battery for electric vehicles: A review," *Energy Storage Materials*, vol. 10. Elsevier, pp. 246–267, Jan. 01, 2018. doi: 10.1016/j.ensm.2017.05.013.

[6] Y. Zheng, Y. Che, X. Hu, X. Sui, D.-I. Stroe, and R. Teodorescu, "Thermal state monitoring of lithium-ion batteries: Progress, challenges, and opportunities," *Prog Energy Combust Sci*, vol. 100, p. 101120, Jan. 2024, doi: 10.1016/j.pecs.2023.101120.

[7] L. H. J. Raijmakers, D. L. Danilov, R.-A. Eichel, and P. H. L. Notten, "A review on various temperature-indication methods for Li-ion batteries," *Appl Energy*, vol. 240, pp. 918–945, Apr. 2019, doi: 10.1016/j.apenergy.2019.02.078.

[8] X. Lin, H. E. Perez, J. B. Siegel, and A. G. Stefanopoulou, "Robust estimation of battery system temperature distribution under sparse sensing and uncertainty," *IEEE Transactions on Control Systems Technology*, vol. 28, no. 3. pp. 753–765, 2020. doi: 10.1109/TCST.2019.2892019.

[9] C. Forgez, D. Vinh Do, G. Friedrich, M. Morcrette, and C. Delacourt, "Thermal modeling of a cylindrical LiFePO4/graphite lithium-ion battery," *J Power Sources*, vol. 195, no. 9, pp. 2961–2968, 2010, doi: 10.1016/j.jpowsour.2009.10.105.

[10] X. Lin *et al.*, "A lumped-parameter electro-thermal model for cylindrical batteries," *Journal of Power Sources*, vol. 257. pp. 12–20, 2014. doi: 10.1016/j.jpowsour.2014.01.097.

[11] Y. Kim, J. B. Siegel, and A. G. Stefanopoulou, "A computationally efficient thermal model of cylindrical battery cells for the estimation of radially distributed temperatures," in *Proceedings of the American Control Conference*, IEEE, Jun. 2013, pp. 698–703. doi: 10.1109/acc.2013.6579917.

[12] R. R. Richardson, S. Zhao, and D. A. Howey, "On-board monitoring of 2-D spatially-resolved temperatures in cylindrical lithium-ion batteries: Part I. Low-order thermal modelling," *J Power Sources*, vol. 326, pp. 377–388, 2016, doi: 10.1016/j.jpowsour.2016.06.103.

[13] M. Sajid, A. A. Hussein, A. Wadi, and M. F. Abdel-Hafez, "An Enhanced Fusion Algorithm With Empirical Thermoelectric Models for Sensorless Temperature Estimation of Li-ion Battery Cells," *IEEE/ASME Transactions on Mechatronics*, vol. 28, no. 2, pp. 621–631, Apr. 2023, doi: 10.1109/TMECH.2023.3235726.

[14] H. Pang, L. Guo, L. Wu, J. Jin, F. Zhang, and K. Liu, "A novel extended Kalman filter-based battery internal and surface temperature estimation based on an improved electro-thermal model," *J Energy Storage*, vol. 41, no. June, p. 102854, 2021, doi: 10.1016/j.est.2021.102854.

[15] Q. Yao, D. D. C. Lu, and G. Lei, "A Surface Temperature Estimation Method for Lithium-ion Battery Using Enhanced GRU-RNN," *IEEE Transactions on Transportation Electrification*, 2022, doi: 10.1109/TTE.2022.3197927.

[16] Y. Zheng, Y. Che, X. Hu, X. Sui, and R. Teodorescu, "Sensorless Temperature Monitoring of Lithium-ion Batteries by Integrating Physics with Machine Learning," *IEEE Transactions on*

Transportation Electrification, pp. 1–1, 2023, doi: 10.1109/TTE.2023.3294417.

[17] O. Ojo, H. Lang, Y. Kim, X. Hu, B. Mu, and X. Lin, "A Neural Network Based Method for Thermal Fault Detection in Lithium-Ion Batteries," *IEEE Transactions on Industrial Electronics*, vol. 68, no. 5, pp. 4068–4078, 2021, doi: 10.1109/TIE.2020.2984980.

[18] A. A. Hussein, "Sensorless Temperature Estimation for Li-Ion Battery Cells: An Overview, Practical Considerations, Challenges and Future Trends," *IEEE Trans Ind Appl*, vol. 59, no. 4, pp. 4598–4609, Jul. 2023, doi: 10.1109/TIA.2023.3259397.

[19] X. Wang *et al.*, "A review of modeling, acquisition, and application of lithium-ion battery impedance for onboard battery management," *eTransportation*, vol. 7, p. 100093, Feb. 2021, doi: 10.1016/j.etran.2020.100093.

[20] K. Mc Carthy, H. Gullapalli, K. M. Ryan, and T. Kennedy, "Review—Use of Impedance Spectroscopy for the Estimation of Li-ion Battery State of Charge, State of Health and Internal Temperature," *J Electrochem Soc*, vol. 168, no. 8, p. 080517, 2021, doi: 10.1149/1945-7111/ac1a85.

[21] S. Ludwig, M. Steinhardt, and A. Jossen, "Determination of Internal Temperature Differences for Various Cylindrical Lithium-Ion Batteries Using a Pulse Resistance Approach," *Batteries*, vol. 8, no. 7, p. 60, Jun. 2022, doi: 10.3390/batteries8070060.

[22] R. R. Richardson and D. A. Howey, "Sensorless Battery Internal Temperature Estimation Using a Kalman Filter with Impedance Measurement," *IEEE Transactions on Sustainable Energy*, vol. 6, no. 4. pp. 1190–1199, 2015. doi: 10.1109/TSTE.2015.2420375.

[23] R. R. Richardson, P. T. Ireland, and D. A. Howey, "Battery internal temperature estimation by combined impedance and surface temperature measurement," *J Power Sources*, vol. 265, pp. 254–261, 2014, doi: 10.1016/j.jpowsour.2014.04.129.

[24] Z. Chen, Y. Zhang, R. Yang, C. Liu, and G. Chen, "Online Internal Temperature Estimation for Lithium-Ion Batteries Using the Suppressed Second-Harmonic Current in Single- Phase DC/AC Converters," *IEEE Transactions on Industrial Electronics*, pp. 1–10, 2024, doi: 10.1109/TIE.2023.3331090.

[25] D. Xiang, C. Yang, H. Li, Y. Zhou, S. Zhu, and Y. Li, "Online Monitoring of Lithium-Ion Battery Internal Temperature Using PWM Switching Oscillations," *IEEE Trans Power Electron*, vol. 38, no. 1, pp. 1166–1177, Jan. 2023, doi: 10.1109/TPEL.2022.3202939.

[26] R. Srinivasan, B. G. Carkhuff, M. H. Butler, and A. C. Baisden, "Instantaneous measurement of the internal temperature in lithium-ion rechargeable cells," *Electrochim Acta*, vol. 56, no. 17, pp. 6198–6204, 2011, doi: 10.1016/j.electacta.2011.03.136.

[27] Robert Richardson, "Impedance-based battery temperature monitoring," Doctoral dissertation, University of Oxford, 2016.

[28] N. Hallemans *et al.*, "Electrochemical impedance spectroscopy beyond linearity and stationarity—A critical review," *Electrochim Acta*, vol. 466, p. 142939, Oct. 2023, doi: 10.1016/j.electacta.2023.142939.

[29] N. Hallemans *et al.*, "Operando electrochemical impedance spectroscopy and its application to commercial Li-ion batteries," *J Power Sources*, vol. 547, p. 232005, Nov. 2022, doi: 10.1016/j.jpowsour.2022.232005.

[30] B. Liebhart, L. Komsiyska, and C. Endisch, "Passive impedance spectroscopy for monitoring lithium-ion battery cells during vehicle operation," *J Power Sources*, vol. 449, p. 227297, Feb. 2020, doi: 10.1016/j.jpowsour.2019.227297.

[31] B. Liebhart, S. Diehl, and C. Endisch, "Sensitivity Analysis of Battery Cell Aging Estimators based on Impedance Spectroscopy regarding Temperature Compensation," in *2020 IEEE Conference on Control Technology and Applications (CCTA)*, IEEE, Aug. 2020, pp. 801–806. doi: 10.1109/CCTA41146.2020.9206395.

[32] J. P. Schmidt, S. Arnold, A. Loges, D. Werner, T. Wetzel, and E. Ivers-Tiffée, "Measurement of the internal cell temperature via impedance: Evaluation and application of a new method," *J Power Sources*, vol. 243, pp. 110–117, 2013, doi: 10.1016/j.jpowsour.2013.06.013.

[33] H. P. G. J. Beelen, L. H. J. Raijmakers, M. C. F. Donkers, P. H. L. Notten, and H. J. Bergveld, "A comparison and accuracy analysis of impedance-based temperature estimation methods for Li-ion batteries," *Appl Energy*, vol. 175, pp. 128–140, 2016, doi: 10.1016/j.apenergy.2016.04.103.

[34] N. S. Spinner, C. T. Love, S. L. Rose-Pehrsson, and S. G. Tuttle, "Expanding the operational limits of the single-point impedance diagnostic for internal temperature monitoring of lithium-ion batteries," *Electrochim Acta*, vol. 174, pp. 488–493, 2015, doi: 10.1016/j.electacta.2015.06.003.

[35] X. Du, J. Meng, J. Peng, and Y. Liu, "A Novel Lithium-Ion Battery Impedance Fast Measurement Method With Enhanced Excitation Signal," *IEEE Transactions on Industrial Electronics*, vol. 70, no. 12, pp. 12322–12330, Dec. 2023, doi: 10.1109/TIE.2023.3234127.

[36] J. Peng, J. Meng, X. Du, L. Cai, and D.-I. Stroe, "A Fast Impedance Measurement Method for Lithium-Ion Battery Using Power Spectrum Property," *IEEE Trans Industr Inform*, vol. 19, no. 7, pp. 8253–8261, Jul. 2023, doi: 10.1109/TII.2022.3217474.

[37] X. Zhu, N. Hallemans, B. Wouters, R. Claessens, J. Lataire, and A. Hubin, "Operando odd random phase electrochemical impedance spectroscopy as a promising tool for monitoring lithium-ion batteries during fast charging," *J Power Sources*, vol. 544, p. 231852, Oct. 2022, doi: 10.1016/j.jpowsour.2022.231852.

[38] W. Han, T. Wik, A. Kersten, G. Dong, and C. Zou, "Next-Generation Battery Management Systems: Dynamic Reconfiguration," *IEEE Industrial Electronics Magazine*, vol. 14, no. 4, pp. 20–31, Dec. 2020, doi: 10.1109/MIE.2020.3002486.

[39] B. Liebhart, S. Diehl, M. Schmid, C. Endisch, and R. Kennel, "Improved Impedance Measurements for Electric Vehicles with Reconfigurable Battery Systems," in *2021 IEEE 12th Energy Conversion Congress & Exposition - Asia (ECCE-Asia)*, IEEE, May 2021, pp. 1736–1742. doi: 10.1109/ECCE-Asia49820.2021.9479060.

[40] R. Teodorescu, X. Sui, S. B. Vilsen, P. Bharadwaj, A. Kulkarni, and D.-I. Stroe, "Smart Battery Technology for Lifetime Improvement," *Batteries*, vol. 8, no. 10, p. 169, Oct. 2022, doi: 10.3390/batteries8100169.

[41] Z. Song, H. Wang, J. Hou, H. F. Hofmann, and J. Sun, "Combined State and Parameter Estimation of Lithium-Ion Battery With Active Current Injection," *IEEE Trans Power Electron*, vol. 35, no. 4, pp. 4439–4447, Apr. 2020, doi: 10.1109/TPEL.2019.2945513.

[42] Y. Zheng, Y. Che, X. Hu, X. Sui, and R. Teodorescu, "Sensorless Temperature Monitoring of Lithium-ion Batteries by Integrating Physics with Machine Learning," *IEEE Transactions on Transportation Electrification*, pp. 1–1, 2024, doi: 10.1109/TTE.2023.3294417.

[43] Y. Zheng, Y. Che, X. Hu, X. Sui, and R. Teodorescu, "Online Sensorless Temperature Estimation of Lithium-Ion Batteries Through Electro-Thermal Coupling," *IEEE/ASME Transactions on Mechatronics*, pp. 1–12, 2024, doi: 10.1109/TMECH.2024.3367291.

[44] P. Gasper, A. Schiek, K. Smith, Y. Shimonishi, and S. Yoshida, "Predicting battery capacity from impedance at varying temperature and state of charge using machine learning," *Cell Rep Phys Sci*, vol. 3, no. 12, p. 101184, Dec. 2022, doi: 10.1016/j.xcrp.2022.101184.

[45] P. Kollmeyer, "Panasonic 18650pf li-ion battery data," *Mendeley Data*, vol. 1, no. 2018, 2018.